Turing-like structures in a functional model of cortical spreading depression

A. Yu. Verisokin* and D. V. Verveyko†
Department of Theoretical Physics, Kursk State University, Radishcheva st., 33, 305000, Kursk, Russia

D. E. Postnov‡
Saratov State University, Astrakhanskaya st., 83, 410012, Saratov, Russia

(Received 26 April 2017; revised manuscript received 6 September 2017; published 18 December 2017)

Cortical spreading depression (CSD) along with migraine waves and spreading depolarization events with stroke or injures are the front-line examples of extreme physiological behaviors of the brain cortex which manifest themselves via the onset and spreading of localized areas of neuronal hyperactivity followed by their depression. While much is known about the physiological pathways involved, the dynamical mechanisms of the formation and evolution of complex spatiotemporal patterns during CSD are still poorly understood, in spite of the number of modeling studies that have been already performed. Recently we have proposed a relatively simple mathematical model of cortical spreading depression which counts the effects of neurovascular coupling and cerebral blood flow redistribution during CSD. In the present study, we address the main dynamical consequences of newly included pathways, namely, the changes in the formation and propagation speed of the CSD front and the pattern formation features in two dimensions. Our most notable finding is that the combination of vascular-mediated spatial coupling with local regulatory mechanisms results in the formation of stationary Turing-like patterns during a CSD event.

DOI: 10.1103/PhysRevE.96.062409

I. INTRODUCTION

Cortical spreading depression (CSD) is a wave of activity that propagates slowly across the brain cortex, which was discovered and first described by Leao [1] more than 60 years ago. CSD along with spreading depolarization events at stroke or injures, as well as migraine waves, is an extreme event in brain physiology. The major phase of these events is accompanied by excessively high neuronal activity, which leads to massive ion redistribution and drastic increase of metabolic demands [2].

In terms of spatiotemporal dynamics, CSD and similar phenomena fall in the field of spatio-temporal pattern formation in active media. The experimentally observed behaviors include retracting waves [3], spiral waves [4,5], and localized moving spots of activity [6].

It is worth mentioning that spreading depolarization events in the brain cortex should be viewed as physiological, rather than "information processing" events. Thus, the modeling studies on the topic form their own research field, which in turn can be split in two.

The first one is represented by the detailed physiological models aimed at verifying the consistency of experimental data and/or testing the proposed physiological pathways [7–11]. These quantitative modeling studies consider the combinations of specific ionic currents.

The second group of modeling studies deals with a phenomenological simplified description of causal pathways and is aimed at reproducing the observed spatio-temporal patterns and contributing to better understanding of the underlying dynamical mechanisms. The first model of this group is the Hodgkin-Grafstein (HG) model proposed in Ref. [12], which is a one-component reaction-diffusion (RD) model with a generic cubic nonlinear term allowing the propagation of an activation wave. In Ref. [13] the retracting waves and spiral waves are reproduced with quantitative two- and six-component RD-type models derived from the balance of major ions. In Ref. [6] the modification and extension of the HG model is suggested in order to explain the experimentally observed dynamics such as spiral waves and moving spots. In Ref. [14] a similar approach is used to construct the four-component CSD model, based on the previous study of the three-component RD model with an additional variable that stands for the accumulation of an extracellular depolarizing agent [15], which fits the needs of CSD modeling well. Note that, unlike in Ref. [14], the models suggested in both Refs. [12] and [6] do not describe the neuronal spiking, being focused on spreading of the CSD front and the formation of specific patterns (moving spots, spiral waves).

While the diffusion in extracellular space is confirmed as the major mechanism of the formation of a propagating CSD front, it was found that some other mechanisms or spatial coupling pathways should also contribute. In Ref. [6] the unspecified nonlocal and delayed coupling are suggested to control the observed patterns. In Ref. [14] the near-boundary dynamics is shown to be essential for the formation of local spots of activity with limited lifetime.

Over the last decades a considerable body of facts has been accumulated regarding cerebral blood flow (CBF) changes during CSD and similar phenomena. It has been shown that arterial (but not venous) vessels show rapid response to the propagation of the CSD front [16]. In Refs. [17,18] it is hypothesized that the observed dilation of blood vessels triggered in the current location of the CSD front can propagate upstream fast. The major local mechanism of such a response is currently understood as propagated vasodilatation [19], utilizing the signaling mechanisms in the endothelial layer.

*ffalconn@mail.ru
†allegroform@mail.ru
‡postnov@info.sgu.ru

Blood flow-related perfusion changes can in turn affect the CSD characteristics, such as the amplitude and duration of depolarization and the propagation velocity [20,21].

The pathways described above are believed to be important for the formation of spatiotemporal patterns of neuronal activity during CSD. However, this problem has currently been addressed in very few modeling studies.

In Ref. [22], a reasonably simplified model was suggested in order to relate the changes in neuronal activity and resulted adjustment of cerebral blood volume. In Ref. [23] basic responses in a single neurovascular unit were modeled. In Ref. [24] the modeling study of metabolic and perfusion effects on CSD is presented. It is shown that different vascular responses to CSD may alter some features of propagated CSD wave.

Recently in Ref. [25] we have proposed the first, to our knowledge, lumped mathematical model of CSD propagation that takes into account spatial coupling not only via redistribution of ions, but also due to vascular responses. Our goal was to simulate the most basic responses of the blood flow network on local changes of vessel radius during the CSD formation. With two types of such responses, the first one being the conducted dilation and the second one being the flow sharing in branching points of the vascular tree, we obtain a six-component reaction-diffusion model equipped with two nondiffusive coupling pathways. Since the pathways newly included in the model provide the additional local feedback loops as well as spatial couplings, its dynamical consequences are not evident. Namely, the biphasic nature of local vascular response can provide both accelerating and slowing down of CSD propagation. The potassium-mediated regulation of the vessel radius provides backward effects not only on neural activity, but also on perfusion rate and, thus, on the regulatory pathway itself. In the current study we address the above issues.

The paper is organized as follows: In the "Model" section we present the model equations with the description of the physiological meaning and dynamical role of each term. In this section we also illustrate the main operating regime for both one- (1D) and two-dimensional (2D) implementation of the model. In the "Results" section we start with the discussion of the possible types of vessel radius response during CSD front propagation, and sensitivity of model dynamics to the choice of control parameters. Our main findings are described in Sec. III C, the formation of stationary Turing-like patterns in respect to the vessel radius and, hence, the blood flow, while the behavior of "conventional" CSD-related variables remains almost unchanged. We discuss the mechanisms of the observed effects, as well as their implications, in the "Conclusions" section.

II. MODEL

Below we describe a set of equations, focusing on the contribution of each term to model dynamics, while more detailed justification of this model can be found in Ref. [25].

A. Physiological basis of the model

The main physiological elements and the flowchart of the developed model are shown in Figs. 1(a) and 1(b), respectively.

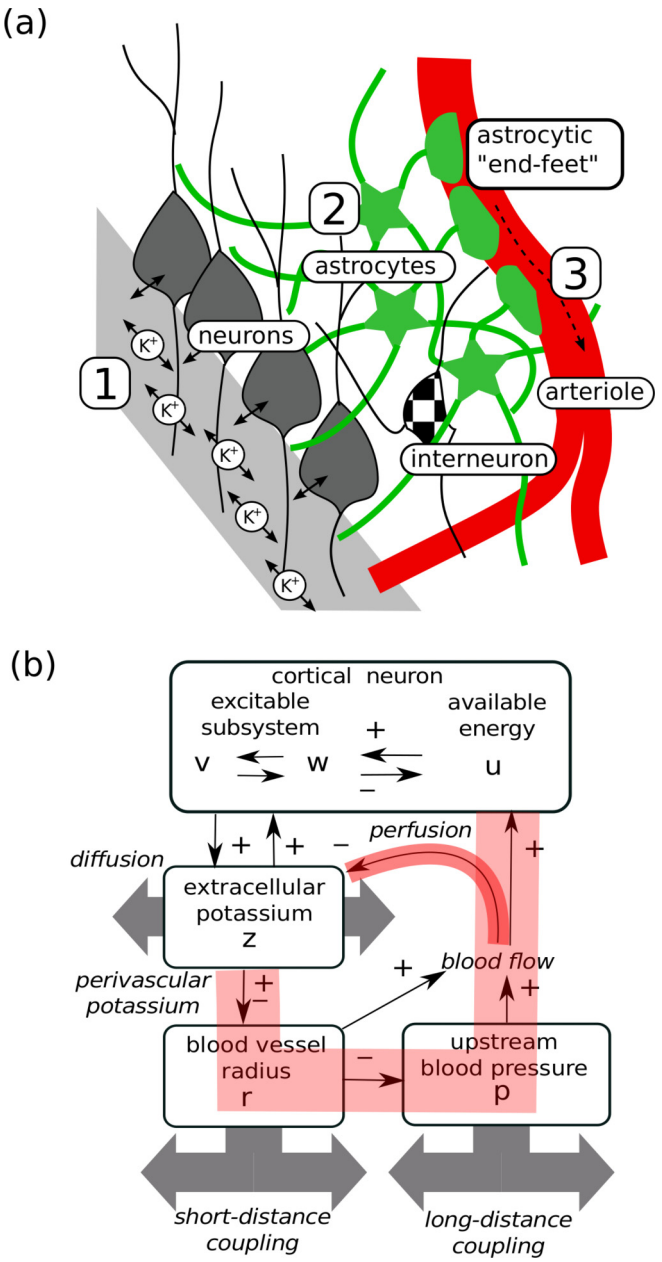

FIG. 1. The schematic representation of modeled pathways (a) and the flowchart of the developed model (b).

In Fig. 1(a) the numbers 1, 2, and 3 label the main modeled pathways for the CSD front propagation:

(1) Firing neurons release potassium to the extracellular space. This in turn provides further depolarization for both firing and neighboring neurons. Thus, neurons reach the maximal firing rate, and this state propagates over neuronal population.

(2) Intensive neuronal firing activity, which is known as neurovascular coupling. In order to maintain the activity each neuron should receive some amount of energy, primarily in the form of oxygen and glucose that are transported from the blood vessels located nearby. Cortical neurons are believed to send a message to the adjacent blood capillaries by means of different pathways, including the astrocyte calcium dynamics [26].

Astrocytes, in turn, have the mechanism for calcium-triggered release of potassium into the perivascular (near-the-blood-vessel) space. This release of potassium affects the state of the vessel smooth muscle cells. Depending on the perivascular potassium concentration reached, both dilation and (at high potassium concentrations) constriction of a vessel can evolve [23,27]. The resulting adjustment of the vessel radius leads to the modulation of the O_2 and glucose amount available for the neuron [22].

(3) There is well-established evidence that the local increase of a blood vessel radius may propagate both upstream and downstream [19]. Such conducted vasodilation (or in some cases vasoconstriction) provides the spatial coupling in the distance range up to 2 mm showing the exponential decay with the distance [28] or the less studied nondecaying pattern similar to the pulse transmission by neurons [29].

Being spatially synchronized over a group of small blood vessels, dilation or constriction inevitably causes blood redistribution in treelike vascular structures: if some location consumes more blood, the neighbors will receive less. It might explain the observed antiphase alterations of CBF [30]. This type of competitive coupling (i) should have larger spatial scale and (ii) in turn might trigger the localized response in distant locations. This type of flow-mediated coupling in kidney was examined in Refs. [31,32]. In the brain cortex such *hemodynamic coupling* has been studied less. However, this pathway may be responsible for experimentally recorded vasodilation *ahead of* the propagated front of intensive neuronal activity [33].

B. Model equations

The physiological pathways outlined above were implemented with the following set of equations:

$$\varepsilon_v \partial_t v = v - v^3/3 - w + z - \mu_n (1-u)^n (v+1)^3 + D\xi(x_0,y_0,t), \tag{1}$$

$$\varepsilon_w(v)\partial_t w = A + Bv - w + \mu_n (1-u)^n + I_{\text{app}}, \tag{2}$$

$$\varepsilon_z \partial_t z = \alpha_z \psi(v) - [1 + k_z(p-p_v)\rho_0 r^4]z + \gamma\left(\partial^2_{xx} z + \partial^2_{yy} z\right), \tag{3}$$

$$\varepsilon_r \partial_t r = 1 + \sum_{x,y}\{W_R(x_0,y_0) q[z(x,y)]\} - r(x_0,y_0), \tag{4}$$

$$\varepsilon_p \partial_t p = 1 - p - (p-p_v)\rho_0 \sum_{x,y}[W_P(x_0,y_0) r^4(x,y)], \tag{5}$$

$$\varepsilon_u \partial_t u = (1-u)(p-p_v)\rho_0 r^4 - \beta_u \psi(v), \tag{6}$$

where

$$\psi(v) = \frac{1}{2}\left[1 + \tanh\left(\frac{v}{v_s}\right)\right], \tag{7}$$

$$\varepsilon_w(v) = \tau_l + \left(\tau_r - \tau_l\right)\psi(v), \tag{8}$$

$$q(z) = c_0 \frac{c_1 - e^{\phi}}{e^{-\phi} + e^{\phi}}, \quad \phi = (c_2 z - c_3)/c_4. \tag{9}$$

The local dynamics is described by six dynamical variables: v, w, z, r, p, and u, the dynamics of which is attached to the specific point (x_0, y_0) on the 2D surface. In spite of the fact that our model is rather lumped and the equations are dimensionless, in order to keep the relation with the original problem, we will discuss the meaning of the control parameters and variables in terms of modeled physiological pathways.

1. Model counterpart of neuronal activity: The spiking subsystem

The first two equations (1) and (2) describe an excitable unit based on the FitzHugh–Nagumo model with the modifications suggested in Ref. [14]. Variables v and w play the roles of an activator and inhibitor, respectively, describing the fast changes of transmembrane voltage and slower recovery of ionic currents. Parameters ε_v, ε_w and A, B set the time scales and the excitability threshold, respectively. Nonlinear terms rated by parameter μ_n introduce the changes in the model behavior depending on the current metabolic stores (variable u). Namely, at low u values the spiking subsystem (1)–(2) becomes nonexcitable, possessing single stable equilibrium at negative v [14].

In Eq. (1), the location-specific and time-dependent function $\xi(x_0,y_0,t)$, scaled by D, provides random uncorrelated fluctuations for each location and serves as a surrogate substitution for a real random-like informational signal processed by a neuron. This term describes the net effect of a large number of spikes received by a neuron. All these signals are the short impulses, which are essentially faster then evoked postsynaptic responses. That is why this "spiking noise" could be considered as (i) "white," i.e., high-frequency noise [34] and has the Gaussian statistics [35]. Thus, we assume that $\xi(x_0,y_0,t)$ is a zero-mean and δ-correlated random process for each point (x_0,y_0):

$$\langle \xi(x_0,y_0,t)\rangle = 0, \tag{10}$$

$$\langle \xi(x_0,y_0,t),\xi(x_0,y_0,t+\tau)\rangle = \delta(\tau). \tag{11}$$

The recovery variable w is essential to provide the spiking behavior of a model neuron (1)–(2) by driving this subsystem back to the resting state, thus being the inhibitor using the terms of activator-inhibitor dynamics. During the formation and propagation of the CSD front, the action of w appears to be effectively blocked since the high value of z clamps the variable v in the positive (excited) state. When the metabolic variable u falls below some critical level, this locking becomes broken, and w can drive the system back to rest.

For a mathematical description of the stimulus that triggers the CSD wave, we use the additive term I_{app} in (2). Experimentally, CSD can be triggered by different methods, so it can be introduced differently in the model. For example, electrostimulation, which depolarizes a neuron, can be modeled as the displacement of its resting state towards the excitation threshold. This is what the additive term I_{app} in Eq. (2) does. Note that the model is capable of spontaneous formation of CSD even at vanishing I_{app}, since there is a persistent spiking process provided by term $D\xi(x_0,y_0,t)$. However, at the standard set of parameters the probability of

such an event is rather small. With introduced negative I_{app} the probability of spontaneous formation of CSD increases since the spiking subsystem approaches the excitation threshold and becomes more sensitive to the noisy term $D\xi(x,y,t)$. Note that essentially the same result can be achieved by means of local increase of variable z; the latter mimics the focal administration of, say, KCl. In terms of model dynamics, the resulted CSD pattern is essentially independent of the specific triggering method, since all of them activate the same positive feedback loop between the v and z variables.

The equation for z describes the accumulation and reuptake of extracellular potassium and in turn affects the excitability of the model neuron acting opposite to w in Eq. (1). The increase of z occurs during each neuronal spike when v becomes positive and $\psi(v) \approx 1$. In other words the term $\alpha_z \psi(v)$ with activator parameter α_z could be considered as the rate of z increasing during neuron firing activity. The reuptake of potassium is modeled with the term $[1 + k_z(p - p_v)\rho_0 r^4]z$, which accounts for both background mechanisms and the contribution from tissue perfusion (see the description of the equations for u and p below). The perfusion value is determined by the parameter k_z. The diffusion term $\gamma(\partial^2_{xx} z + \partial^2_{yy} z)$ describes the diffusion of potassium from the extracellular space to other locations; here γ is the diffusion coefficient for z variable.

The essentials of the noise-driven dynamics of a three-component reaction-diffusion model similar to (1)–(3) were analyzed in Ref. [15].

2. Modeling of blood vessel responses

One of the most notable pathways of neuronal regulation of the local blood flow supply is based on transporting of excessive extracellular potassium by astrocytes to their endfeet with subsequent release into the perivascular space. This pathway was implemented in the model studies [22,23]. Note that while the CSD formation is accompanied by a calcium wave propagating in parallel through the astrocyte network, it has been shown that this is an attribute, rather than the mechanism, of CSD propagation [36,37]. It has also been demonstrated that vessel radius changes follow the extracellular potassium changes showing quite a small delay [38]. In view of the above, in our model we omit the mediating role of astrocytes and assume that perivascular potassium concentration changes instantly and in fixed proportion to the changes of z. This allows us to describe the potassium-induced changes of blood vessel radius r with empirical function $q(z)$ [Eq. (9) and Fig. 2], which shape resembles the simulation results [23].

Considering the value $q(z)$ at the point (x_0, y_0) as a local "vascular driving force," the total "vascular forcing" received at this location is provided by the net contribution from nearby located vessel segments. We describe it by means of the term $\sum_{x,y}\{W_R(x_0,y_0)q[z(x,y)]\}$ in Eq. (4), being the weighted sum of $q(z)$ values within some area calculated using the window function $W_R(x_0,y_0)$ with width W_{R_0}. In this way we implement short-distance coupling via the conducted vasoreactivity, which describes the resulted changes in the radius of the blood vessel by means of simple first-order kinetics.

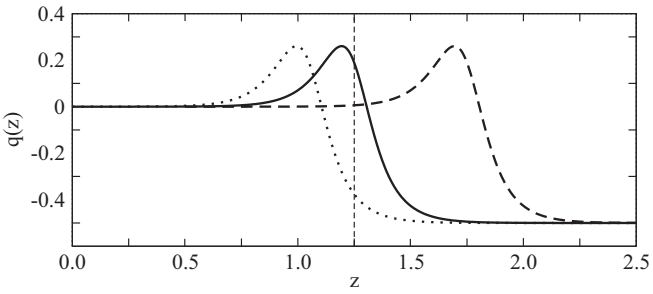

FIG. 2. Function $q(z)$ [see Eq. (9)] describing the biphasic response of a blood vessel radius to the value of perivascular potassium concentration. The depicted specific curve was calculated at $c_0 = 0.5$, $c_1 = 1.78$, $c_2 = 20.0$, $c_4 = 2.0$, $c_3 = 23.0$, 25.0, 35.0 (dotted, solid, dashed lines), respectively. The vertical dashed line shows the typical z value during the active stage of the CSD pattern

3. Blood flow sharing

Equation (5) describes the local changes of blood flow governed by changes of the vessel radius in the given and neighboring locations. It has been derived using the following assumptions:

(1) For each point (x_0, y_0) there is some upstream branching point B of blood vessels that feeds this location.

(2) This branching point receives the blood flow from the upstream large arterial vessel and feeds the bunch of smaller vessels, including the current location.

(3) The relative contribution of vessels in the bunch is maximal for the current location (x_0, y_0) and decreases with the increase of the distance from that point [39].

(4) The downstream venous pressure is constant and the same for all vessels in the bunch.

On the basis of the above stated, pressure P_B in the branching point is governed by the simple flow balance

$$C_B \frac{dP_B}{dt} = (P_{\text{art}} - P_B)/R_{\text{art}} - (P_B - P_{\text{ven}})/R_B, \qquad (12)$$

where C_B is compliance, P_{art} is constant upstream arterial pressure, R_{art} stands for hydrodynamic resistance from arterial vasculature to B, P_{ven} is constant downstream venous pressure, and R_B denotes total hydrodynamic resistance of the bunch of adjustable vessels.

To simplify Eq. (12) we multiply it by $R_{\text{art}}/P_{\text{art}}$, denote $C_B R_{\text{art}}/P_{\text{art}}$ as ε_p, and introduce the dimensionless pressures $p = P_B/P_{\text{art}}$, $p_v = P_{\text{ven}}/P_{\text{art}}$. Since hydrodynamic resistance R according to the Poiseuille law is inversely proportional to the fourth power of the radius, one can denote $R(x_0,y_0) = R_0(x_0,y_0)(r_0^4/r^4)$, where R_0 corresponds to the rest value of vessel radius r_0. For the sake of simplicity, we assume that r_0 and, hence, R_0 are the same for all vessels, and denote $\rho_0 = R_{\text{art}}/R_0$. With this, the total downstream flow from the branching point reads

$$J = (p - p_v)\rho_0 \sum_{x,y}[W_P(x_0,y_0)r^4(x,y)]. \qquad (13)$$

Here the relative contribution of vessels in the bunch is determined by the window function $W_P(x_0,y_0)$ with width W_{P_0}.

With all the above, we get Eq. (5), where the input and output flows are represented by terms $(1-p)$ and Eq. (13), respectively. Note that the expression $J_(p-p_v)\rho_0 r^4(x_0,y_0)$ gives the flow through the considered location (x_0,y_0) and thus can be used to estimate the perfusion rate in Eq. (3).

4. Metabolic stores

Equation (6) describes the process of expenditure and refilling of metabolic resources. It is derived from the assumption that the current location receives primary metabolic substances (oxygen, glucose) by means of ingoing flow with concentration C_0, and consumes some amount C_{spike} per unit time during each neuronal spike. The resulting local concentration C is washed out from the attached volume L by the outgoing flow (which is the same as the ingoing one).

In terms of our dimensionless model, we define a new variable $u = C/C_0$ and denote $\varepsilon_u = LR_{\text{art}}/P_{\text{art}}$, $\beta_u = C_{\text{spike}}R_{\text{art}}/P_{\text{art}}$. With this, the maximal (unity) concentration of primary metabolic resources is brought by the input flow $(p-p_v)\rho_0 r^4(x_0,y_0)$. Then the output flow washes out the resources with current concentration of u. The consumption is quantified by β_u multiplied by the total duration of time that a neuron spends in a high-v state when $\psi(v)\approx 1$.

As has already been mentioned above, at $u\approx 1$, the value of u has little effect on the dynamics. When it drops to a certain critical level, the spiking subsystem [Eqs. (1)–(2)] turns to the nonexcitable regime, which mimics what happens for a real neuron if the ATP pump fails to maintain normal ionic gradients.

C. Computational implementation of the model

The set of equations described in the previous section was integrated numerically by the explicit method (the fourth order Runge-Kutta method adopted for SDE) both on a 1D (linear) grid and on irregular-bounded and inhomogeneous 2D patterns. The numerical algorithm to perform such simulations has been chosen according to Ref. [40] and previously used in Refs. [14,41]. In brief, this method allows us to prepare the hand-drawn pictures in indexed colors and assign the specific model equations or the specific parameter choice, as well as a coupling type, to each of these colors.

The typical set of control parameters used in simulations is shown in Table I. The adequate choice of the window functions W_R and W_P is actually an issue, since with it we actually map the complex topology of the brain vasculature on the continuous medium of the model. In this study we simply assume that mutual contribution of the two points of the model medium decreases with increasing distance and becomes negligible if the distance between points exceeds a certain value. To meet these assumptions we use the Bartlett window functions (triangular window) in Eqs. (4) and (5):

$$W_{1D}(x) = 1 - \frac{|x-x_0|}{w_0}, \tag{14}$$

$$W_{2D}(x,y) = 1 - \frac{\sqrt{(x-x_o)^2+(y-y_0)^2}}{w_0}, \tag{15}$$

where x_0, y_0 define the center of the window and w_0 is the window width (see Table I).

TABLE I. Set of parameter values for model 1–5.

ε_v	μ	n	τ_l	α_z	W_{R_0}
0.04	3.0	4.0	1.5	1.25	3
A	B	ε_z	τ_r	c_0	W_{P_0}
0.5	1.1	2.5	1.0	0.5	10
ε_r	ε_u	p_v	β_u	c_2	D
5.0	800.0	0.1	0.2	20.0	0.003
ε_p	γ	c_1	c_3	k_z	
1.0	0.07	1.73	23.2	0.32	
ρ_0	c_4	I_{app}			
0.5	2.0	−1.0			

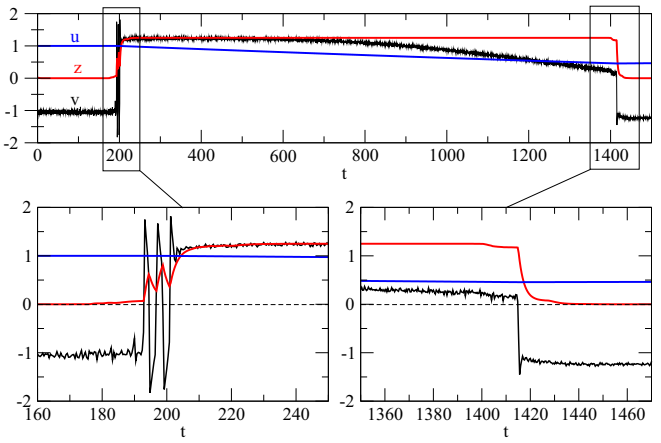

FIG. 3. The time courses of variables v, z, and u showing the CSD-like behavior at the selected location (10th unit of 20) for 1D implementation of model (1)–(9). Inserts show the details of transitions at the leading and rear edges of the CSD front passing this location. $k_z = 0, c_3 = 35, D = 0.004$, other parameters are according to Table I.

D. Main operating regime

Below we will illustrate the core of model behavior. In Fig. 3 we show representative time courses of variables recorded at the selected location in the center of 1D implementation of the model. The top panel shows the complete course of evolution of the modeled CSD event, while the two bottom panels provide the detailed view of what happens during its formation and decay. One can see that the CSD event is characterized by the high level of variables v and z being maintained during long enough time ≈1200, while variable u slowly decreases. Let us term it an "activated state," since it represents the maximal achievable level of neuronal activity. The development of this activated state is precursored by the gradual rise of z (the left bottom panel) provided by its diffusion from the nearby area already occupied by the approaching CSD front. Since the increase of z reduces the excitation threshold, at some moment the spiking subsystem (1)–(2) of the model switches to self-sustained oscillations (three peaks are visible) and then to a permanent activated state. The termination of the activated state (the right bottom panel in Fig. 3) is caused by changes of the dynamical features of the spiking subsystem, which, in

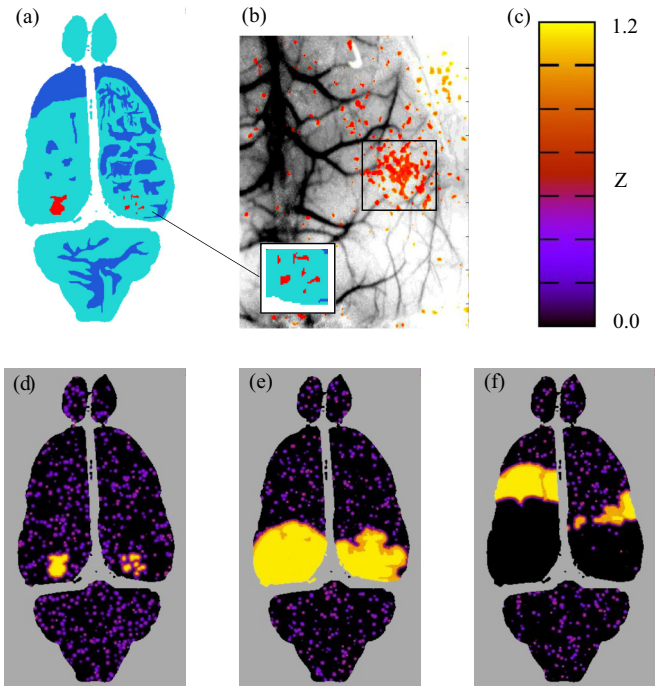

FIG. 4. Full-scale simulations using model (1)–(9). (a) An artificial manually created 2D template is used for simulations. Light and dark blue areas correspond to different choices of k_z: $k_z = 0$ and 25, respectively. Red shows the stimulation sites, where $I_{\text{app}} = -1.0$ during $\Delta t = 10.0$ (otherwise $I_{\text{app}} = 0$). (b) An example of experimentally recorded whisker stimulation response in mouse brain that provides the motivation for stimulation sites' configuration. (Image courtesy of D. D. Postnov, Univ. of Copenhagen.) (c) Color bar for the variable z. (d, e, f) Three representative snapshots taken at $t = 15$, 700, and 1560, respectively. $c_3 = 24.7$, $D = 0.0043$, $\alpha_z = 1.15$, $\varepsilon_u = 300$; other parameters are according to Table I.

turn, are governed by the slow decrease of u. As discussed in Ref. [14], at this transition both excitable and bistable features of the spiking subsystem disappear, so no oscillations occur and all model variables converge to the single and stable equilibrium state.

In Fig. 4 the representative simulation course on an irregular-bounded 2D template is given in order to show the similarity of model behavior with the experimental observations of CSD. Specifically, in Fig. 4(a) we show the computational template, which resembles the shape of a rat brain and uses its natural sectioning to illustrate the variants of model behavior with and without additional stimulus applied to trigger the CSD pattern. The stimulated area is given in red (medium gray), while the simulated areas with normal and increased value of perfusion (parameter k_z) are colored in light and dark blue (light and dark gray).

The left and right "hemispheres" differ in (i) k_z inhomogeneity patterns and (ii) the shape of stimulated area, since we believe it might be important at the stage of initiation of the CSD pattern. Some argumentation to use such a fragmented stimulus area is provided in Fig. 4(b), where the experimentally recorded CBF response in mice brain is visible as a group of scattered spots.

The bottom row of panels in Fig. 4 exemplifies simulation results showing the snapshots of z on the (x, y) plane taken subsequently at time moments $t = 15$ (d), 700 (e), 1560 (f) and depicted according to the color bar in panel (c). One can find that in the absence of stimulation all the template segments show the uncorrelated noise-induced firing pattern: multiple small spots covering the template segments visualize the small splashes of z caused by irregular and not propagated noise-triggered spikes of the fast subsystem. This is an image of a "normal" cortex state, when no large-scale patterns of neuronal dynamics occur.

An additional stimulation applied to the depicted areas by means of setting $I_{\text{app}} = -1.0$ during $\Delta t = 10.0$ (otherwise $I_{\text{app}} = 0$) triggered the formation of a CSD-like event: the front of switching to an activation state propagated far beyond the activation sites and occupied all available space. Note that in those template segments that have no spatial connection with stimulated sites, no such behavior occurred during a long simulation time. Another important observation is the completely dark zones in the rear of the moving activity area, being the image of "exhausted" (or depressed) neuronal tissue, that temporarily lost the excitable features. The visible difference between the shape of the left and the right wave front segments is caused by passing the areas with a different perfusion rate (different k_z value); the underlying behavior is discussed below.

III. RESULTS

The simulated behavior described above confirms that the core part of the model (1)–(9) is capable of reproducing the main dynamical features of the CSD event, including the uncorrelated noise-induced firing pattern in a "normal" state, the spreading area of persistent neuronal depolarization, and the depressed state afterwards. Below we focus on dynamic consequences of the blood-flow related part of the model, Eqs. (4), (5), and (6), in order to reveal the actions and features of the introduced pathways.

A. Vessel radius response types

First, we consider how the blood vessel radius r can respond to the approaching CSD front. For this purpose we (i) block influence of the flow on z dynamics selecting $k_z = 0$ in order to break the possible feedback contribution, and (ii) select the set of c_3 values at the full-scale activation of z.

According to Eq. (3), if v switches to a persistent activated state, $v > 0$, then z reaches a value $\approx\alpha_z$. However, the resulted changes of r essentially depend on the specific $q(z)$ shape.

We consider the numerical solution of the model (1)–(9) in a 1D distributed system, so it is suggested that the CSD process occurs in the homogeneous medium which consists of 100 elements. In Fig. 5 i is an element number. Here and below (Figs. 5–8) the diffusion operator of z in Eq. (3) for each element i was calculated in the form of finite differences $\gamma(z_{i-1} + z_{i+1} - 2z_i)$. We choose the Neumann boundary condition for such a 1D system, i.e., there is no diffusion of z through the boundaries and no contribution to the coupling terms in Eqs. (4) and (5).

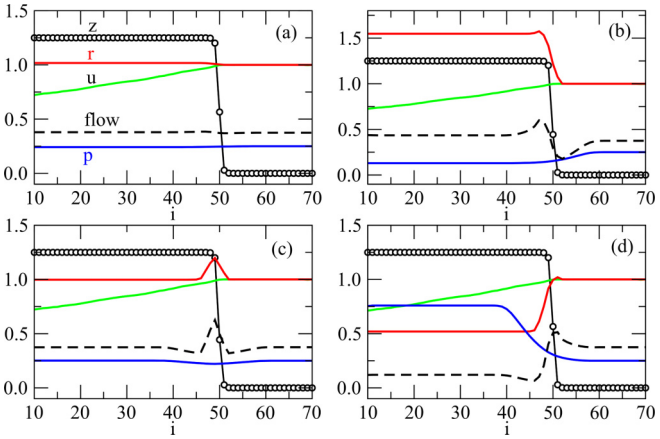

FIG. 5. 1D model implementation. Spatial profiles of variables z, u, r, and p for different c_3 values at the same position ($i = 50$) of the leading edge of the CSD front that moves from the left to the right and is visible as a sharp rise of z. $c_3 = 35.0, 25.0, 23.9, 23.0$ for (a), (b), (c), and (d), respectively. $k_z = 0$, $c_3 = 35$, $D = 0.004$, other parameters are represented in Table I.

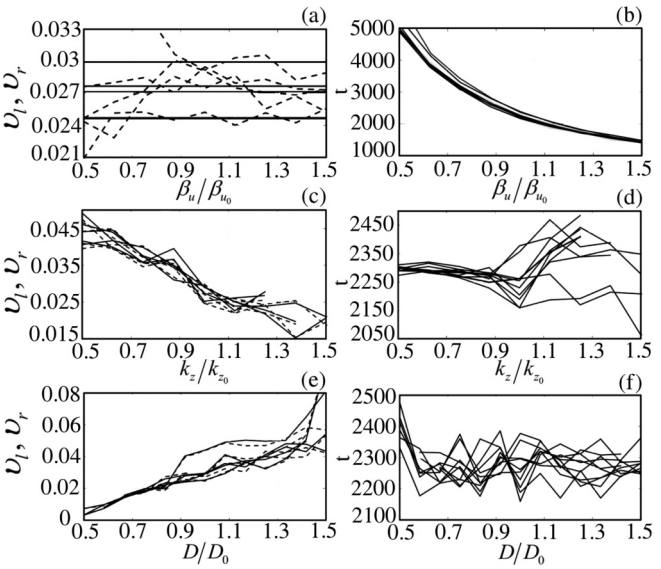

FIG. 6. Model parametrization. In each panel, the set of lines of the same type exemplifies the set of simulation runs at different random sequences; see the text for details. Three rows characterize the sensitivity of simulated CSD pattern for three essential model parameters: β_u, k_z, and D. Two panels in each row describe the measured velocities if the leading and the rear fronts of the CSD pattern (left) and the corresponding duration T of the active phase are calculated in a selected location. The parameter set is according to Table I.

In Fig. 5 different variants of r response to the rise of z (depicted with open circles) are shown versus c_3 value:

(a) At $c_3 = 35.0$ the radius variable r practically does not react to a z rise; there is no pronounced vascular response [Fig. 5(a)].

(b) At $c_3 = 25.0$ [Fig. 5(b)] r increases to $r \approx 1.6$, since the function $q(z)$ is positive (see Fig. 2) at the reached z values. In terms of the original physiological problem it means that the blood vessel dilates. The close inspection of curves shows that the rise of r starts slightly before the depolarization wave reaches this location, which is pretty consistent with experimental findings.

(c) At $c_3 = 23.9$ the reached value of $q(z)$ is equal to zero, so the vascular response is neutral: we observe a short radius r dilation caused by the transition through the positive segment of $q(z)$, but then r returns to its original value [Fig. 5(c)].

(d) At $c_3 = 23.0$ r decreases to $r \approx 0.5$, since at this parameter selection the negative segment of $q(z)$ is reached [Fig. 5(d)]. In terms of the cerebral blood flow it means considerable vasoconstriction, which might complicate the tissue recovery. As was hypothesized in Refs. [22,23], it might be caused by the excessive potassium release into perivascular space.

B. Parametrization of CSD pattern

In this section we investigate how the introduced model pathways affect the main features of CSD pattern: the propagation speed for the leading and rear edges as well as the resulted duration of a hyperactive state of the neuronal medium. We select the perfusion rate k_z, resources consumption rate β_u, and noise intensity D as the control parameters that affect the dynamics of CSD wave.

Note that our model is essentially stochastic, and at vanishing D the CSD front will simply not appear. Moreover, specific features (say, nucleation time) of a triggered front are also dependent on a specific random sequence $D\xi(x_0, y_0, t)$. Thus, we consider the model behavior at different values of parameters using the same set of time series of $D\xi(x_0, y_0, t)$. The simulations are performed using 1D implementation of the model consisting of 300 units.

The obtained results for different values of β_u, k_z, and D parameters at different random $\xi(x_0, y_0, t)$ sequences are shown in Fig. 6.

The left column in Fig. 6 represents the velocities of the leading and rear fronts of the CSD wave. The velocity values are given in a number of units traversed by the wave during one dimensionless unit of time; for example, the velocity value 0.02 means that the wave passes 100 units over 5000 dimensionless units of time. Solid and dashed lines taken for different random sequences correspond to the leading and the rear edge propagation speeds, respectively. The right column of the figure shows the dependence of the CSD wave duration (i.e., its active phase) on the control parameters. In all cases the horizontal axis shows the decimal share of the basic β_{u_0}, k_{z_0} and D_0 parameters from Table I.

Inspection of Fig. 6 shows that the velocity of the leading CSD front depends on the random $\xi(x_0, y_0, t)$ sequences, but not on β_u values. It can be explained by the fact that slowly varying energy variable u after the CSD wave formation is still close to its initial value $u \approx 1$ and cannot considerably alter the behavior of "neuronal" equations of the model. In contrast, the velocity of the rear edge appears to be scattered over the value for the leading edge since the deactivation of a neuron is mainly determined by variable u, but can be accelerated or slowed down due to additional activator v fluctuations caused by $\xi(x_0, y_0, t)$.

Duration T of the whole CSD wave decreases exponentially with the increasing of parameter β_u [Fig. 6(b)], since in activated state $\psi(v) = 1$ the dynamics of u is essentially governed by the fist-order linear ODE [Eq. (6)].

Variation of parameter k_z has no direct impact on the velocity of the neuron energy change, but contributes considerably to the front propulsion by means of the z variable equation.

For the leading edge increased k_z prevents fast accumulation of z in the units ahead of the front position. Since during an activated state z is fixed and the duration of this phase is governed by decreased u, specific k_z has little effect on time lag T between the leading and rear fronts. Thus, both velocities show similar dependence: the increase of k_z slows down both the leading and rear edges as can be seen in Fig. 6(c).

The increase of parameter D directly affects fluctuations of variable v and thus leads to the increase of the leading and rear edge velocities [Fig. 6(e)], as it accelerates both the depolarization of a neuron and its return to the rest state. Thus, T appears to be scattered and does not show any specific trend [Fig. 6(f)]. The dependence of the velocities on the intensity parameter D is close to linear. The range of wave duration values and values of the leading and rear edges velocities is associated with the stochasticity of the process, and this range increases with the increase of D.

C. Perfusion rate and CSD pattern features

The specific feature of our model is that it counts not only local neurovascular regulatory pathways, but also spatial coupling mediated by the blood vessels and blood flow sharing. Above we have shown that the same rise of z can trigger different responses of r. The observed behavior looks quite similar to experimentally observed response patterns [33,42]. Note that this is the direct consequence of the specific choice of function $q(z)$, so it might be considered as a model verification, rather than a prediction.

There are, however, less evident features provided by the vascular-related model pathways. If one examines Fig. 1 again, neuronal activity controls the change of r; the latter affects the flow, which, in turn, controls both the energy supply for a neuron (arrow pointed to u in figure) and washing out the extracellular potassium (arrow pointed to z). Thus, this pathway forms two feedback loops: the first one includes the slowest model variable u and has well-predictable features (the higher the flow, the better the energy supply and the longer the active phase of CSD pattern). The other feedback loop has a less evident effect. In real brain cortex the relaxation of the elevated extracellular potassium level is provided by the variety of pathways, including the uptake by neurons and glial cells and the diffusion and the washing out by the tissue perfusion. In our model the latter mechanism is implemented by means of the term $k_z(p - p_v)\rho_0 r^4$, which mediates the degradation rate for z. This, in turn, can either decrease or increase r, depending on the specific z value and the specific parameters of $q(z)$.

The performed simulations using the individual model (1)–(9) do not reveal any substantial changes of dynamical regimes due to this mechanism. However, for 1D and 2D model implementations the situation is different.

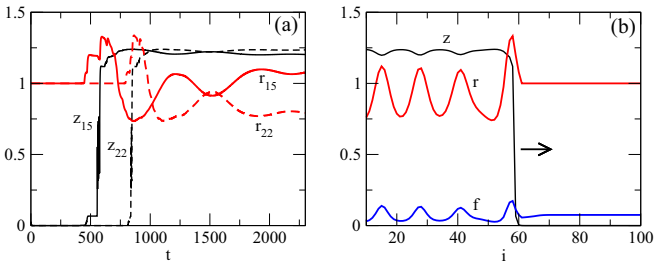

FIG. 7. Standing pattern formation. (a) Time courses of z and r for two elements of a 1D array: the 15th (solid lines) and the 22th (dashed lines). Both r curves show oscillations which are, however, finally converged to different values. (b) In spatial domain, the 1D array shows the formation of a wavelike stationary pattern in respect to r, which is also reflected in spatial profiles of flow f and z. Arrow indicates the direction of SCD-front propagation. $D = 0.0025$; other parameters are according to Table I.

Figure 7 illustrates the obtained results using a 1D array of 60 units. Figure 7(a) shows time series of z and r obtained for the 15th and 22th units of the array. The moment of time when the propagating CSD front approaches a unit is indicated by a sharp rise of z. One can see that the response of r on this sharp rise looks similar for both units, being the damped oscillations converging to the new value of r. However, the achieved new values are substantially different for the 15th and the 22th units. Figure 7(b) shows what happens in the spatial domain. One can find that the propagating CSD front is tailed by the spatially periodic profile of vessel radius r and flow f. We have found that the spatial scale of this periodic profile is approximately equal to the doubled width of the window function in Eq. (6). The key role of spatial coupling is confirmed by means of simulation runs with blocked coupling via r: no spatially periodic patterns have been found.

Figure 8 illustrates how the revealed behavior depends on parameter ρ_0, which physiological meaning is the ratio of upstream and local blood vessel resistance, while dynamically this parameter quantifies the response of p to flow modulation. In order to improve the visualization of CSD wave propagation we perform simulation runs using the 300-unit 1D array. At $\rho_0 = 0.25$ (top panel) both temporal and spatial periodicity are not pronounced, while r transients are attached to the leading and rear edges of the CSD front. At higher $\rho_0 = 0.4$ (middle panel) both temporal oscillations and a spatial periodic pattern can be detected, as was discussed above. Finally, at high $\rho_0 = 0.7$ (bottom panel) no temporal oscillations can be observed, but a spatially periodic structure appears immediately after transients on the leading edge of the front and persists during the active phase of the CSD event.

The described results clearly show that both r and p variables, each with an attributed spatial coupling pathway, contribute to the formation of a periodic standing pattern. The natural question arises, "How will this effect manifest itself for 2D model implementation?" Figure 9 shows representative snapshots taken from a 100×100 lattice with the CSD front triggered at the left edge. The boundary conditions are set as an "anatomical block," being "no-flux" (Neumann) boundary for z and "empty area" (no contribution to coupling terms) for r and p. The parameters are set as in Fig. 7, except k_z which is

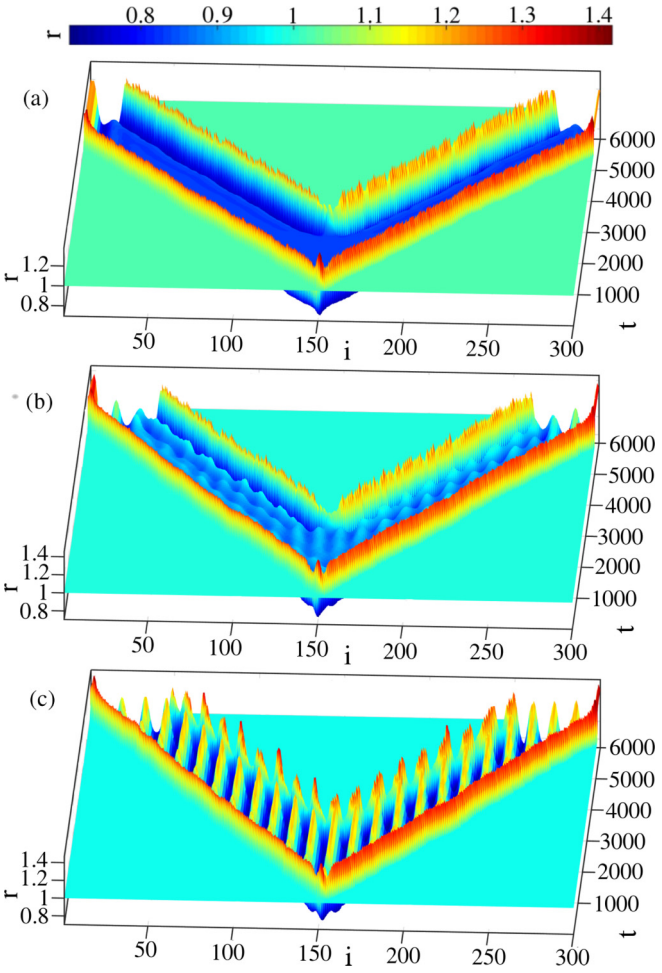

FIG. 8. Space-time plots for r showing the formation of Turing-like stationary patterns. (a), (b), and (c) have been obtained at $D = 0.0025$, $\rho_0 = 0.25$, 0.4, and 0.7, respectively. Other parameters are according to Table I.

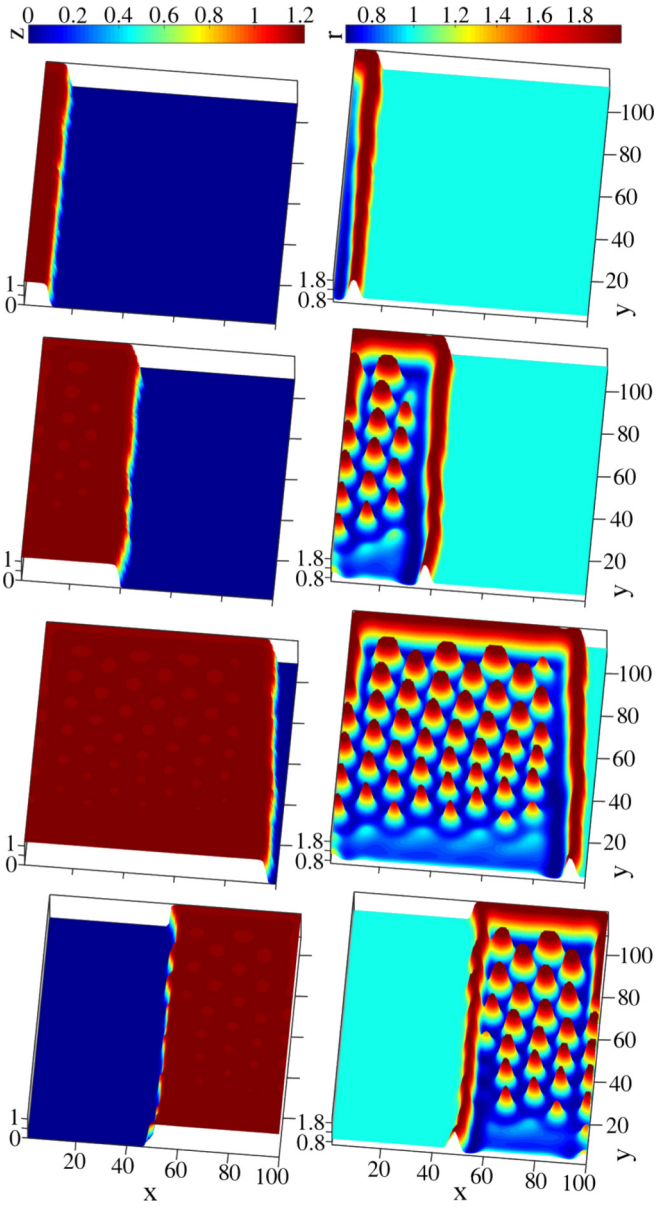

FIG. 9. Formation of Turing-like stationary pattern in two dimensions. Left and right columns show the snapshots of z and r, respectively, calculated on a 100×100 grid and taken simultaneously. Four rows correspond to four selected moments of time, $t = 100$, 500, 1250, and 1750 from the top to the bottom, respectively. Parameters are set as in Fig. 7: $k_z = 0.4$, $\alpha_z = 1.22$, $\rho_0 = 1$, $\varepsilon_u = 400$; the other parameters are according to Table I. An additional stimulation was applied to the left edge of the template by means of setting $I_{\text{app}} = -1.0$ during $\Delta t = 10.0$ (otherwise $I_{\text{app}} = 0$). This and similar examples are provided in the Supplemental Material [39].

set to be increasing linearly from $k_z = 0.1$ at $y = 0$ to $k_z = 0.8$ at $y = 100$.

The top row (a) shows the just-triggered CSD front at $t = 100$. While z shows uniform stitching to the high-value state (left panel), r first rises but afterwards falls to the values lower than those at the rest. The second (b) and third (c) rows show the snapshots taken at the moments $t = 500$ and $t = 1000$ when the CSD front propagates about half the distance and almost all available space, respectively. While z behavior is essentially the same as in (a), r forms the 2D counterpart of 1D periodic structure, being the population of spots of high values which fills the space already occupied by the CSD front. Clearly, this self-organized pattern is not perfectly periodic, but rather fills the space in some "optimal" way. The gap between the continuous line of transients at the leading edge of the CSD front and the spots population means that spots start to grow only after z is switched to its high ($\approx\alpha_z$) value. The introduced gradient of k_z manifests itself via different sizes of spots, as well as via behavior at the boundaries: at $y = 0$, where k_z is low, there is no formation of r structure at all, while at $y = 0$, where k_z is high, r has persistent high values. The bottom row (d) taken at $t = 1750$ illustrates the "washing out" of spatio-temporal structures by the rear egde of CSD front. After a transient rise r values return to their original level $r = 1$.

Speaking in terms of dynamics, the emergence of self-organized patterns described above might be explained by the combined action of the following:

(1) Since function $q(z)$ has the negative slope at medium z values, it can support instability being included into feedback

loop: rise (fall) of z can induce the decrease (increase) of perfusion term and thus support the further rise (fall) of z.

(2) Spatial coupling via r supports cooperative behavior for the nearest neighbors.

(3) Spatial coupling via p is of competitive type and involves more remote locations than coupling via r.

As we have shown in Figs. 8 and 9, the discussed pattern formation can be observed for the ranges of relevant control parameters, rather than at their unique combination, so it appears to be structurally stable; see also Ref. [39].

IV. CONCLUSIONS

To summarize, we have shown that the model reproduces the main dynamical mechanisms of the formation and evolution of spatial temporal patterns during cortical spreading depression, namely, (i) uncorrelated noise-induced firing in rest, (ii) persistent neuronal depolarization during the "active" phase of CSD, and (iii) a depressed state afterwards, when the model medium temporarily losses excitability and does not respond to noisy stimuli. The simulated types of vascular response are also in qualitative agreement with the known experimental findings.

From the dynamical viewpoint, we have shown that newly modeled pathways form the additional feedback loops, and thus they are capable of the new types of behavior. The most notable finding is the formation of spatially periodic Turing-like structures, which are the result of combined action of two nonlocal coupling pathways.

From the physiological point of view, the obtained results suggest that a certain combination of involved pathways, namely, potassium-mediated regulation of the arteriolar radius and washing out of extracellular potassium by means of perfusion, defines the specific pattern of blood flow changes during CSD. Although our results can hardly be experimentally tested directly (due to the strong spatial inhomogeneity of the spatial parameters), nonmonotonic oscillating intensity of the blood flow or the vessel radius during a CSD regime are reported in a number of experimental studies of CSD, and it appears to be an established fact.

Our main conclusion in terms of physiological interpretation can be formulated in the following way: In addition to actual neural activity, there are dynamic mechanisms that significantly influence the formation of CBF patterns, which are therefore not uniquely related to neuronal activity.

Currently it is difficult to say to what extent the revealed effect is relevant to real dynamics of cerebral circulation, since the gap between the flat and homogeneous model environment and the structure of a real cortex is too large. Nevertheless, we believe that our findings contribute to understanding which mechanisms can cause the uncertainness of the relationship between measured changes of the cerebral blood flow and underlying neuronal activity, which can be so ambiguous and variable under different conditions, as becomes increasingly evident for neurophysiologists and clinicians.

ACKNOWLEDGMENTS

This work was made possible by RFBR grant 15-32-51178. D.V.V. acknowledges support from the Ministry of Education and Science of the Russian Federation within research project 3.9499.2017, included in the basic part of research funding assigned to Kursk State University. D.E.P. acknowledges support from the Ministry of Education and Science of the Russian Federation, contract 3.5507.2017/VU.

[1] A. A. P. Leão, J. Neurophysiol. **7**, 359 (1944).
[2] C. Ayata and M. Lauritzen, Physiol. Rev. **95**, 953 (2015).
[3] M. Shibata and J. Bures, J. Neurobiol. **5**, 107 (1974).
[4] N. Gorelova and J. Bures, J. Neurobiol. **14**, 353 (1983).
[5] M. Dahlem and S. Muller, Exp. Brain. Res. **115**, 319 (1997).
[6] M. A. Dahlem, R. Graf, A. J. Strong, J. P. Dreier, Y. A. Dahlem, M. Sieber, W. Hanke, K. Podoll, and E. Schöll, Physica D **239**, 889 (2010).
[7] H. C. Tuckwell and R. M. Miura, Biophys. J. **23**, 257 (1978).
[8] H. Kager, W. J. Wadman, and G. G. Somjen, J. Neurophysiol. **84**, 495 (2000).
[9] B. E. Shapiro, J. Comput. Neurosci. **10**, 99 (2001).
[10] W. Yao, H. Huang, and R. Miura, Bull. Math. Biol. **73**, 2773 (2011).
[11] G. Somjen, H. Kager, and W. J. Wadman, J. Comput. Neurosci. **25**, 349 (2008).
[12] B. Grafstein, in *Brain Function. Cortical Excitability and Steady Potentials*, edited by M. A. B. Brazier (University of California Press, Berkeley, 1963), p. 87.
[13] H. C. Tuckwell, AIP Conf. Proc. **1028**, 46 (2008).
[14] D. E. Postnov, D. D. Postnov, and L. Schimansky-Geier, Brain Res. **1434**, 200 (2012).
[15] D. E. Postnov, F. Muller, R. B. Schuppner, and L. Schimansky-Geier, Phys. Rev. E **80**, 031921 (2009).
[16] M. Bouchard, B. Chen, S. Burgess, and E. Hillman, Opt. Express **17**, 15670 (2009).
[17] B. Chen, M. Bouchard, A. McCaslin, S. Burgess, and E. Hillman, Neuroimage **54**, 1021 (2011).
[18] B. Chen, M. Kozberg, M. Bouchard, M. Shaik, and E. Hillman, JAHA **3**, e000787 (2014).
[19] F. Gustafsson and N.-H. Nolstein-Rathlou, Acta Physiol. Scand. **167**, 11 (1999).
[20] J. Dreier, Nat. Med. **17**, 439 (2011).
[21] I. Sukhotinsky, E. Dilekoz, M. Moskowitz, and C. Ayata, J. Cereb. Blood Flow Metab. **28**, 1369 (2008).
[22] W. Gibson, L. Farnell, and M. Bennett, Neurocomputing **70**, 1674 (2007).
[23] H. Farr and T. David, J. Theor. Biol. **286**, 13 (2011).
[24] J. C. Chang, K. C. Brennan, D. He, H. Huang, R. M. Miura, P. L. Wilson, and J. J. Wylie, PLoS ONE **8**(8), e70469 (2013).
[25] A. Y. Verisokin, D. Verveyko, and D. Postnov, Proc. SPIE **9917**, 99171Z (2016).
[26] G. Carmignoto and M. Gómez-Gonzalo, Brain Res. Rev. **63**, 138 (2010).
[27] M. Koide, A. D. Bonev, M. T. Nelson, and G. C. Wellman, Proc. Natl. Acad. Sci. U. S. A. **109**, E1387 (2012).
[28] G. J. Crane, T. O. Neild, and S. S. Segal, Microcirculation **11**, 425 (2004).

[29] X. F. Figueroa, C.-C. Chen, K. P. Campbell, D. N. Damon, K. H. Day, S. Ramos, and B. R. Duling, Am. J. Physiol. Heart Circ. Physiol. **293**, H1371 (2007).

[30] P. B. Jones, H. K. Shin, D. A. Boas, B. T. Hyman, M. J. Moskowitz, C. Ayata, and A. K. Dunn, J. Biomed. Opt. **13**, 044007 (2008).

[31] D. J. Marsh, A. S. Wexler, A. Brazhe, D. E. Postnov, O. V. Sosnovtseva, and N.-H. Holstein-Rathlou, Am. J. Physiol. Renal. Physiol. **304**, F88 (2013).

[32] D. D. Postnov, D. E. Postnov, D. J. Marsh, N.-H. Holstein-Rathlou, and O. V. Sosnovtseva, Bull. Math. Biol. **74**, 2820 (2012).

[33] K. C. Brennan, L. Beltrán-Parrazal, H. E. López-Valdés, J. Theriot, A. W. Toga, and A. C. Charles, J. Neurophysiol. **97**, 4143 (2007).

[34] W. Softky and C. Koch, J. Neurosci. **13**, 334 (1993).

[35] V. Anishchenko, V. Astakhov, A. Neiman, T. Vadivasova, and L. Schimansky-Geier, *Nonlinear Dynamics of Chaotic and Stochastic Systems. Tutorial and Modern Developments*, Springer Series in Synergetics (Springer, New York, 2007).

[36] T. A. Basarsky, S. N. Duffy, R. D. Andrew, and B. A. MacVicar, J. Neurosci. **18**, 7189 (1998).

[37] N. Zhou, G. R. J. Gordon, D. Feighan, and B. A. MacVicar, Cereb. Cortex **20**, 2614 (2010).

[38] A. Witthoft and G. E. Karniadakis, J. Theor. Biol. **311**, 80 (2012).

[39] See Supplemental Material at http://link.aps.org/supplemental/10.1103/PhysRevE.96.062409 for The figure file Vessels.png shows the further details on spatial coupling via flow sharing, namely, how the 3D vascular tree is "mapped" on the model plane.

The set of movies provide an animated representation of Touring-like patterns formation discussed in the main text. Movie_1 corresponds to Fig. 9.

[40] D. E. Postnov, D. D. Postnov, and R. Zhirin, The "AGEOM_CUDA" software for simulation of oscillatory and wave processes in two-dimensional media of arbitrary geometry on the basis of high-speed parallel computing on graphics processing unit technology CUDA. RF registration certificate no. 2012610085 (in Russian) (2012).

[41] F. Muller, L. Schimansky-Geier, and D. E. Postnov, Ecol. Compl. **14**, 21 (2013).

[42] J. C. Chang, L. L. Shook, J. Biag, E. N. Nguyen, A. W. Toga, A. C. Charles, and K. C. Brennan, Brain **133**, 996 (2010).